APPLIED PHYSICS

Centimeter-scale hole diffusion and its application in organic light-emitting diodes

Shihao Liu[1,2], Jiaming Zhang[1], Chunxiu Zang[1], Letian Zhang[1], Wenfa Xie[1]*, Chun-Sing Lee[2]*

In conventional organic light-emitting diodes (OLEDs), current balance between electron and hole transport regions is typically achieved by leakage of the major carrier through the devices or by accumulation of the major carrier inside the devices. Both of these are known to reduce performances leading to reduction of efficiency and operation stability due to exciton-polaron annihilation, etc. We found that hole diffusion in a centimeter-scale can be achieved in a PEDOT:PSS layer via composition and interface engineering. This ultralong distance hole diffusion enables substantially enhanced hole diffusion current in the lateral direction perpendicular to the applied electric field in typical organic optoelectronic devices. By introducing this lateral hole diffusion layer (LHDL) at the anode side of OLEDs, reduced carrier accumulation, improved efficiency, and enhanced operation stability are demonstrated. The application of the LHDL provides a third strategy for current balancing with much reduced harmful effects from the previous two approaches.

INTRODUCTION

While full-color organic light-emitting diode (OLED) displays have been widely commercialized in the past decade, commercial products of OLED solid-state lighting are still rare. One important reason is that OLEDs, especially high-efficiency phosphorescent OLEDs, do have a common disadvantage that their efficiencies show severe roll-off at high brightness (1–9). It is thus important to address this issue for promoting OLEDs' lighting applications. The "efficiency roll-off" issue is caused by different nonlinear and complicated processes related to organic semiconductors' intrinsic properties (9–11). For organic semiconductors, hole drifting mobilities in hole-transporting materials are typically several orders of magnitude higher than electron mobilities in electron-transporting materials (9, 10, 12). It is generally considered that these mobility differences would lead to unmatched electron and hole currents. Fave et al. (13) have shown that there are two possible scenarios in typical OLEDs. In the first situation, after electron-hole recombination, the surplus carriers (typically hole) will flow through the whole devices. These leakages of the major carriers not only waste energy without generating light but can also decrease operation lifetime. For example, Aziz et al. (14) have shown that leakage of hole current can cause degradation of tris(8-hydroxyquinoline)aluminum(III) (Alq_3) in a prototypical N,N'-bis(naphthalen-1-yl)-N,N'-bis(phenyl)-benzidine (NBP)/Alq_3 device. In many high-efficiency devices, hole-blocking layers are thus inserted to suppress the hole leakage. This leads to the second scenario that excessive holes would accumulate inside the devices, leading to built-in electric fields, which would suppress the hole current and finally achieve balanced currents at electron and hole transport regions. However, these accumulated holes can form polarons and can quench excitons via exciton-polaron annihilation, leading to decreased efficiency and operation lifetime (15–24). It can be seen that in either scenario, both efficiency and operation lifetime are harmfully affected. The key question here is that before we can develop materials with matching electron and hole mobilities, is there a third scenario beyond the above two described by Fave et al. (13)?

Inspired by a milestone discovery of Forrest et al. (25, 26), in this work, we show that a third scenario is possible via introducing current diffusion flow in the lateral direction (i.e., perpendicular to the applied electric field). So far, almost all studies of OLEDs are mainly focused on the carrier dynamics along the direction of electric field, namely, the drifting of carriers perpendicular to the planar devices (27–29). However, charge carriers can also diffuse in all directions, including perpendicular to the electric field, as carrier "diffusion" is driven by concentration gradient and is independent of the electric field (30). Recently, Forrest et al. (25) showed a breakthrough that lateral electron diffusion in centimeter scale can be achieved in a doped C_{60} channel at room temperature. This centimeter-scaled electron diffusion is of critical importance for understanding fundamental physics in organic optoelectronic devices and can be applied for making charge-coupled devices (31). On the one hand, Leo et al. (32, 33) constructed an OLED by using an electron lateral transport layer with a conductivity of 4 S/cm and observed emission spreading of ~300 μm outside the anode-cathode overlapping region. On the other hand, this long-range diffusion for hole has not been reported.

In this work, we demonstrated that hole diffusion in centimeter length scale can be achieved in poly(3,4-ethylenedioxythiophene)-poly(styrenesulfonate) (PEDOT:PSS) layers via composition and interface engineering. This ultralong scale hole diffusion is further exploited to address the issue of efficiency roll-off in OLEDs. It was found that lateral hole diffusion beyond the cathode-anode overlapping region can redistribute carriers and induce additional electron injection from the cathode/organic interface. This leads to effective reduction of hole accumulation inside the device and thus reduces efficiency roll-off. The device also shows over two times of operation lifetime enhancement comparing with the corresponding device without a lateral hole diffusion layer (LHDL). Last, we also demonstrate this by incorporating a LHDL in a white phosphorescent OLED.

RESULTS

Properties of conventional devices without LHDL

Figure 1A shows a schematic view of carrier flows of an operating OLED driven by a direct current (DC) power source. Because of the laws of

[1]State key Laboratory of Integrated Optoelectronics, College of Electronics Science and Engineering, Jilin University, Changchun 130012, People's Republic of China. [2]Center of Super-Diamond and Advanced Films (COSDAF) and Department of Chemistry, City University of Hong Kong, Hong Kong SAR 999077, People's Republic of China.
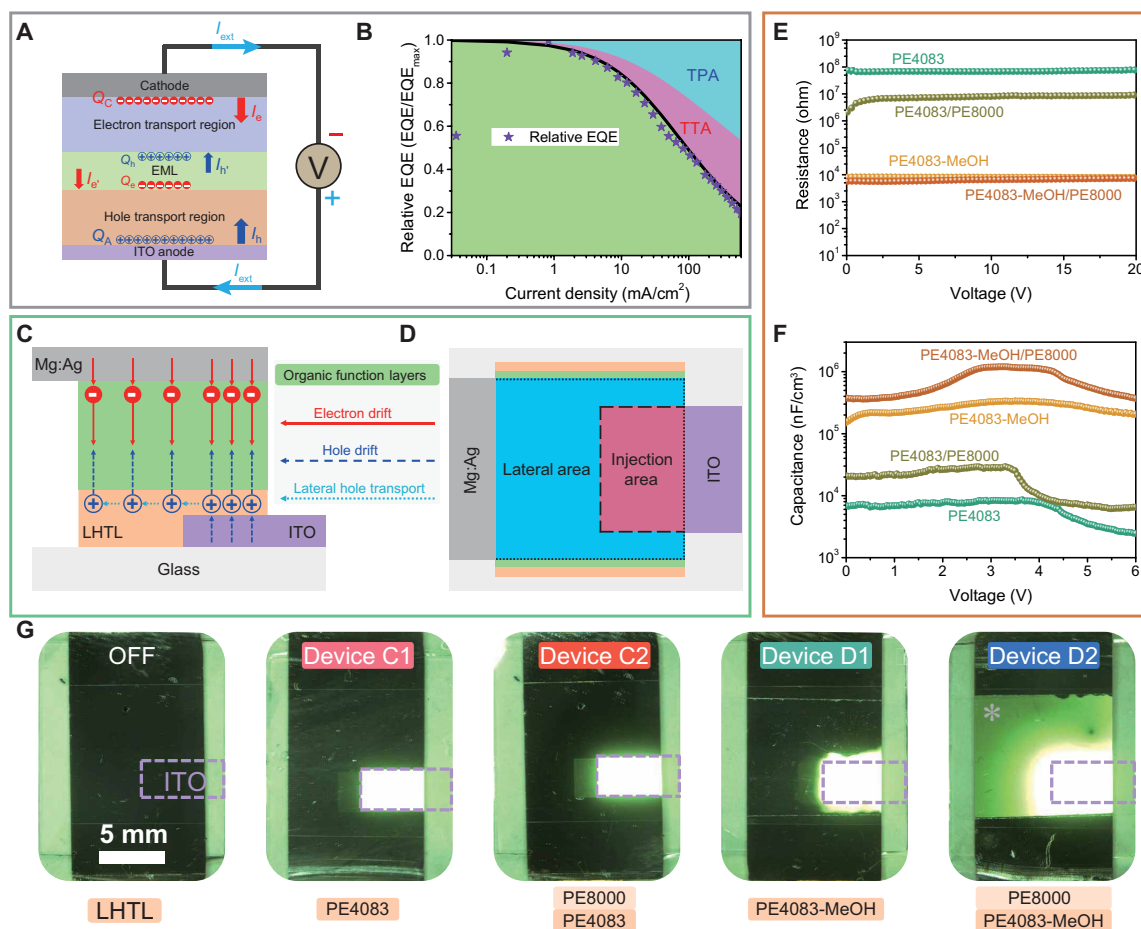*Corresponding aurhor. Email: xiewf@jlu.edu.cn (W.X.); apcslee@cityu.edu.hk (C.-S.L.)

Fig. 1. Design of the LHDL. (A) Schematic view of carrier flows of an operating OLED driven by a DC power source; blue, red, and celeste arrows, respectively, represent directions of hole flows, electron flows, and currents; I_h and I_e are, respectively, the injected hole and electron currents at the electrode/organic interfaces. $I_{h'}$ and $I_{e'}$ are the leakage currents of hole and electron beyond the recombination zone, respectively. I_{ext} is the electric current across the OLED. Q_A and Q_h are hole charges at the surface of anode and in the device interior, respectively. Q_C and Q_e are the corresponding electron charges. **(B)** Theoretically calculated contributions of TTA and TPA to EQE loss in device C1 as a function of current density. Experimentally measured relative EQE is shown as symbol ★.**(C)** Side-view schematic diagram of an OLED with a lateral hole transport layer and **(D)** its top view. **(E)** Lateral resistance and **(F)** capacitance per unit volume characteristics of different types of PEDOT:PSS layers. **(G)** Top-view images of devices C1, C2, D1, and D2 under 6 V.

conservation of charge and continuity of electric current, there is only a fixed electric current I_{ext} in the whole OLED circuit (Fig. 1A), including the OLED itself. The I_{ext} is the net rate of flow of holes and/or electrons, and the direction of I_{ext} (celeste arrows) is defined as the direction of hole flows (blue arrows) and the opposite direction of electron flows (red arrows). Because of exciton radiative recombination, most holes and electrons would be neutralized by each other and not contribute to the I_{ext} beyond the recombination zone. Thus, the I_{ext} of hole transport region consists of the injected hole current I_h and the electron leakage $I_{e'}$, while that of electron transport region is contributed by the injected electron current I_e and the hole leakage $I_{h'}$. In many high-efficiency devices (34–36), carrier blocking layers are inserted to suppress the leakage currents ($I_{e'} \approx 0$, $I_{h'} \approx 0$). Then, there is a current balance between the hole and the electron transport regions for these OLED

$$I_{ext} = I_h = I_e \qquad (1)$$

However, for organic semiconductors, hole-drifting mobilities in hole-transporting materials are typically several orders of magnitude higher than electron mobilities in electron-transporting materials (9, 10, 12). In this case, carrier accumulations inside devices would replace the current leakages for balancing currents of the hole and the electron transport regions (13).

First, a green phosphorescent OLED with a conventional device structure of indium tin oxide (ITO), PEDOT:PSS (30 nm), di-[4-(N,N-di-p-tolyl-amino)-phenyl]cyclohexane (TAPC; 30 nm), 4,4′,4″-tris(carbazol-9-yl)triphenylamine (TCTA; 5 nm), 4,4′-bis(carbazol-9-yl)biphenyl [CBP; 10 weight % (wt %)], tris(2-phenylpyridine)iridium(III) [Ir(ppy)₃; 30 nm], 1,3,5-tri[(3-pyridyl)-phen-3-yl]benzene (TmPyPB; 50 nm), lithium fluoride (LiF; 1 nm), Mg (10 wt %), and Ag (100 nm) was fabricated and called device C1. Characteristics of device C1 are given in the Supplementary Materials (fig. S1). Relative external quantum efficiency (EQE) with respect to the maximum EQE (EQE$_{max}$) of the device is shown with ★ symbols in Fig. 1B. It can be seen that EQE of the device decreases

considerably when the current density is higher than 1 mA/cm^2. Only about 20% of the EQE_{max} can be maintained when the current density is 600 mA/cm^2. Actually, we have prepared devices using different combinations of a common anode buffer layer of PEDOT:PSS and a hole buffer interlayer of TCTA (fig. S3A). Figure S3 shows that these layers have little help in addressing the efficiency roll-off and give no apparent performance enhancement at high current densities. The severe EQE loss at high current densities in typical phosphorescent OLEDs has been attributed to triplet-polaron annihilation (TPA) and triplet-triplet annihilation (TTA) (9, 10, 17, 18). Following the approach of Leo *et al.* (9) and with reference to the parameters (fig. S2A and table S1), we proceed to determine their relative contributions by analyzing densities of triplets (n_T) and polaron (n_P) at steady state. Calculated relative EQE losses due to TTA and TPA are respectively shown as pink and cyan areas in Fig. 1B. Calculated densities of triplet and polaron at different current densities are given in fig. S2B.

As shown in Fig. 1A, TPA dominates the quenching process across the whole current range. This phenomenon can be attributed to excessive hole accumulation caused by the unmatched hole and electron transporting abilities of the organic layers. To confirm this, we prepare a hole-only (C1h) and an electron-only (C1e) devices by modifying the structure of device C1 (fig. S4). Figure S5A shows that current density of device C1h is much higher than that of device C1e. From this result, it can be reasonably considered that the hole and electron transporting abilities of device C1 are highly unmatched (hole dominated). We then measured the capacitance-voltage characteristic of device C1 (fig. S5B). It can be seen that upon carrier injection (at 2.8 V, point a′), capacitance of device C1 shows an initial increase as voltage increases. This is mostly attributed to hole accumulation in the emitting layer based on the discussion in note S1.

Using the "Marburg model" (fig. S6A) (13, 37), the reason of carrier accumulation in device C1 is explored in note S2. In the operating hole–dominant device C1 (fig. S6B), the recombination current I_R can be expressed as

$$I_R = I_h - I_{h'} - \frac{dQ_h}{dt} = I_e \qquad (2)$$

where I_h and I_e are, respectively, the injected hole and electron currents at the electrode/organic interfaces. $I_{h'}$ is the leakage hole current beyond the recombination zone. Q_h is the accumulated hole charges inside the device. Because of efficient hole-blocking abilities of TmPyPB, $I_{h'}$ can be approximated to zero for device C1. Thus, the balance of hole and electron currents is mainly achieved via the term dQ_h/dt. Upon carrier injection (fig. S6B), Q_h increase steadily such that internal potential distribution will be affected. The potential difference (E_h) across hole transport region will decrease, leading to a decreased I_h. Last, enough Q_h is accumulated (i.e., $dQ_h/dt = 0$) and leads to a dynamic equilibrium between hole and electron currents ($I_h = I_e$). Under this dynamic equilibrium, internal electric field distribution is highly uneven. For example, Fave *et al.* (13) showed that E_e can be over three times higher than E_h. Given that the electric field for typical OLEDs is high ($>10^7$ V/m), a considerable number of holes would accumulate in the device interior (10^{11} to 10^{12} cm^{-2}, in reference to our result as shown in fig. S5B). The accumulated holes finally lead to serious TPA in device C1 (Fig. 1B).

Design of the LHDL

To address the issue of excessive hole accumulation, we proposed to introduce a lateral hole current I_L by inserting a lateral hole transport layer (LHTL) between ITO and organic function layers, as shown in Fig. 1 (C and D). The I_L is anticipated to generate an additional electric field helping to extract electrons from the cathode side. As discussed in note S3 (fig. S6C), we show that after introducing the LHTL, it is possible to achieve hole-electron current balance without involving (or with much reduced) hole accumulation. However, note S3 also shows that the LHTL-induced current balance only works under the assumption that the lateral current I_L is obtained via diffusion from the LHTL layer at the anode-cathode overlapping region instead of injection from the ITO. Further evidence supporting this assumption is provided in the later parts of the paper.

PEDOT:PSS is exploited for applications as the lateral transport layer because its conductivity can be changed over a wide range by adjusting its composition and configuration (fig. S7). Figure 1D shows lateral resistivities (fig. S8) of different types of PEDOT:PSS films, including PE4083 (PEDOT:PSS Clevios P VP AI 4083, 30 nm), PE4083/PE8000 bilayer (PEDOT:PSS Clevios P VP: AI 4083, 30 nm/ CH 8000, 30 nm), PE4083-MeOH (methanol-treated PE4083), and PE4083-MeOH/PE8000. Details on preparation of these PEDOT:PSS films are given in the experimental section. As shown in Fig. 1E, untreated PEDOT:PSS films (PE4083, PE4083/PE8000) have higher resistivities, while treatment with methanol (MeOH) can substantially decrease their resistivities. PEDOT:PSS has simultaneously high conductivity and capacitance (Fig. 1, E and F). Holes can be stored at the interface between the conducting PEDOT-rich phase and the insulating PSS rich phase (38, 39). Figure 1F shows that the capacitance of PEDOT:PSS can be increased over two orders of magnitudes upon treatments. The voltage dependence of capacitance is considered to be related to the two-phase system of PEDOT:PSS. The PEDOT:PSS should be treated as two-phase system consisting of PEDOT and PSS chains. The PEDOT:PSS aqueous emulsion is stable because the water-soluble PSS in excess surrounds the PEDOT:PSS particles. It is reasonably considered that carrier blocking and confining abilities of the external PSS surrounding the inner PEDOT:PSS is influenced by the bias voltage and, thus, the capacitance.

Devices C1, C2, D1, and D2 were then prepared using PE4083, PE4083/PE8000, PE4083-MeOH, and PE4083-MeOH/PE8000, respectively, as shown in fig. S9. Figure 1G shows images of the devices operating at 6 V. It can be seen that the emitting area in devices C1 and C2 is limited to the cathode-ITO overlapping region. Apparent emission spreading out of the cathode-ITO overlapping region can be observed in devices D1 and D2. Apparently, the conductivities of PE4083 and PE4083/PE8000 layers are not high enough to allow adequate lateral hole current I_L such that devices C1 and C2 behave as conventional devices with no observable emission spreading. The high conductivity of PE4083-MeOH and PE4083-MeOH/PE8000 in devices D1 and D2 enables enhanced lateral hole current I_L and thus emission spreading. In particular, emission can still be obtained in device D2 from regions of centimeter scale away from the cathode-ITO overlapping region. It can be noted that device D2 shows much wider emission spreading than device D1 (Fig. 1G), although their PEDOT:PSS layers have similar lateral resistances and conductivities (~4 S/cm; Fig. 1E and fig. S10). This suggests that the capacitance (Fig. 1F) of the PEDOT:PSS layer might have influences on the lateral current I_L. Thus, we further measure the impedance spectra (Fig. 2) of the PEDOT:PSS layers in devices C2 and D2 with the
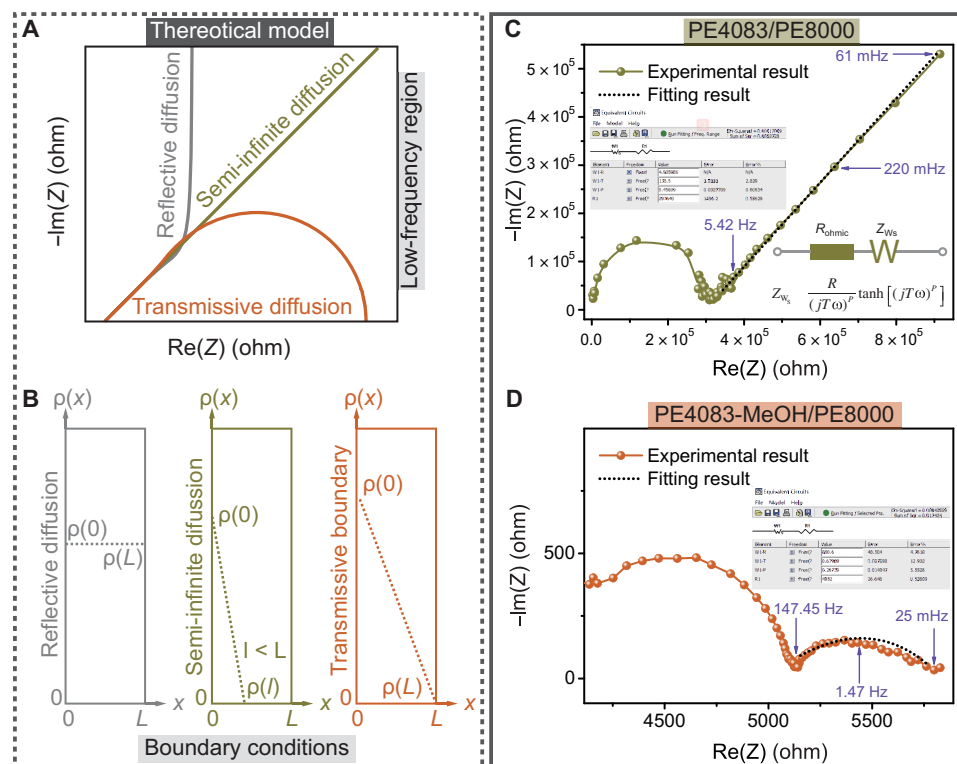
Fig. 2. Impedance spectroscopy of PEDOT:PSS films. (**A**) Schematic diagram of lateral real versus imaginary impedance spectra of reflective or transmissive finite-length linear diffusion and semi-infinite linear diffusion in theory and (**B**) their boundary conditions; here, ρ represents the charge concentration. Experimental impedance spectra of (**C**) PE4083/PE8000 and (**D**) PE4083-MeOH/PE8000 layers. The insets show their equivalent circuits and fitting parameters.

configuration as shown in fig. S8. Reflective or transmissive finite-length linear diffusions and semi-infinite linear diffusion are characterized by the theoretically derived complex plane plots (Fig. 2A) of Warburg impedance (*40*). Their boundary conditions are shown in Fig. 2B. The experimental results (Fig. 2, C and D) show that hole transport in the PH4083/PH8000 film belongs to a semi-infinite linear diffusion with a semi-infinite boundary while that in the PH4083-MeOH/PH8000 film belongs to a finite-length diffusion with a transmissive boundary. It indicates that diffusion of the PE4083/PE8000 is only bounded by an electrode on one side while that of the PE4083-MeOH/PE8000 is not. Results of the PE4083 and PE4083-MeOH films (fig. S11) are similar to those of their corresponding bilayer PEDOT:PSS films. The hole diffusivity, *D*, of the PE4083-MeOH/PE8000 film is then estimated as ~3 × 10^{-3} cm^2/s (note S4), which is over two orders of magnitude higher than that (lower than 1.8 × 10^{-5} cm^2/s) of the PE4083/PE8000 film. We can thus reasonably consider that lateral carrier transport in the PEDOT:PSS layers belongs to hole diffusion behavior as a result of the combination of their high conductivity and capacitance properties. For this reason, these PEDOT:PSS layers are hereafter referred as LHDL.

We then measured transient electroluminescence (EL) of devices C2 and D2 from a far field such that emissions both within and outside the cathode-ITO overlapping region can be collected (Fig. 3A). It can be seen that the transient EL in device C2 matches well to the electrical pulse showing little delay. The transient EL in device D2 shows two rising stages. The initial rise (<10 μs) is nearly identical to that of device C2 (see inset of Fig. 3A). The delayed rise is much

slower and emerges when device C2 maintains a steady state. Transient EL from device D2 was then measured from the spot marked with "*" in Fig. 1G, which is about 0.57 cm outside the cathode-ITO overlapping region, using a longer electrical pulse of 480 μs (fig. S12). No appreciable EL signal can be observed before 90 μs (see magnified region in the inset of fig. S12). This suggests that emission from this spot requires diffusion and accumulation of carriers from a long distance away. Thus, the initial and delayed emissions shown in Fig. 3A correspond to emissions within and outside the cathode-ITO overlapping region, respectively. However, transient current characteristics (Fig. 3B) show that the external currents of devices C2 and D2 remain unchanged after initial charging process (i.e., after 10 μs) for activating the OLED. This suggests that the I_L for driving the delayed EL rise is not directly injected from the ITO anode.

The delayed EL (Fig. 3A and fig. S13) can be more reasonably explained by lateral hole diffusion in the PEDOT:PSS layer driven by the hole concentration gradient. When the bias is first applied, carrier movement will be dominantly controlled by the vertical electric field. There will be little lateral current I_L as there is no apparent carrier density gradient initially. The PEDOT:PSS will be steadily charged up with an increasing hole concentration. Upon fully charged, there will be a large enough lateral hole concentration gradient driving a lateral hole current I_L. The laterally diffuse holes would then induce additional electron injection from the cathode giving rise to the delayed EL. With this understanding, the hole-electron current balance can be achieved via lateral hole diffusion (as discussed in note S3)
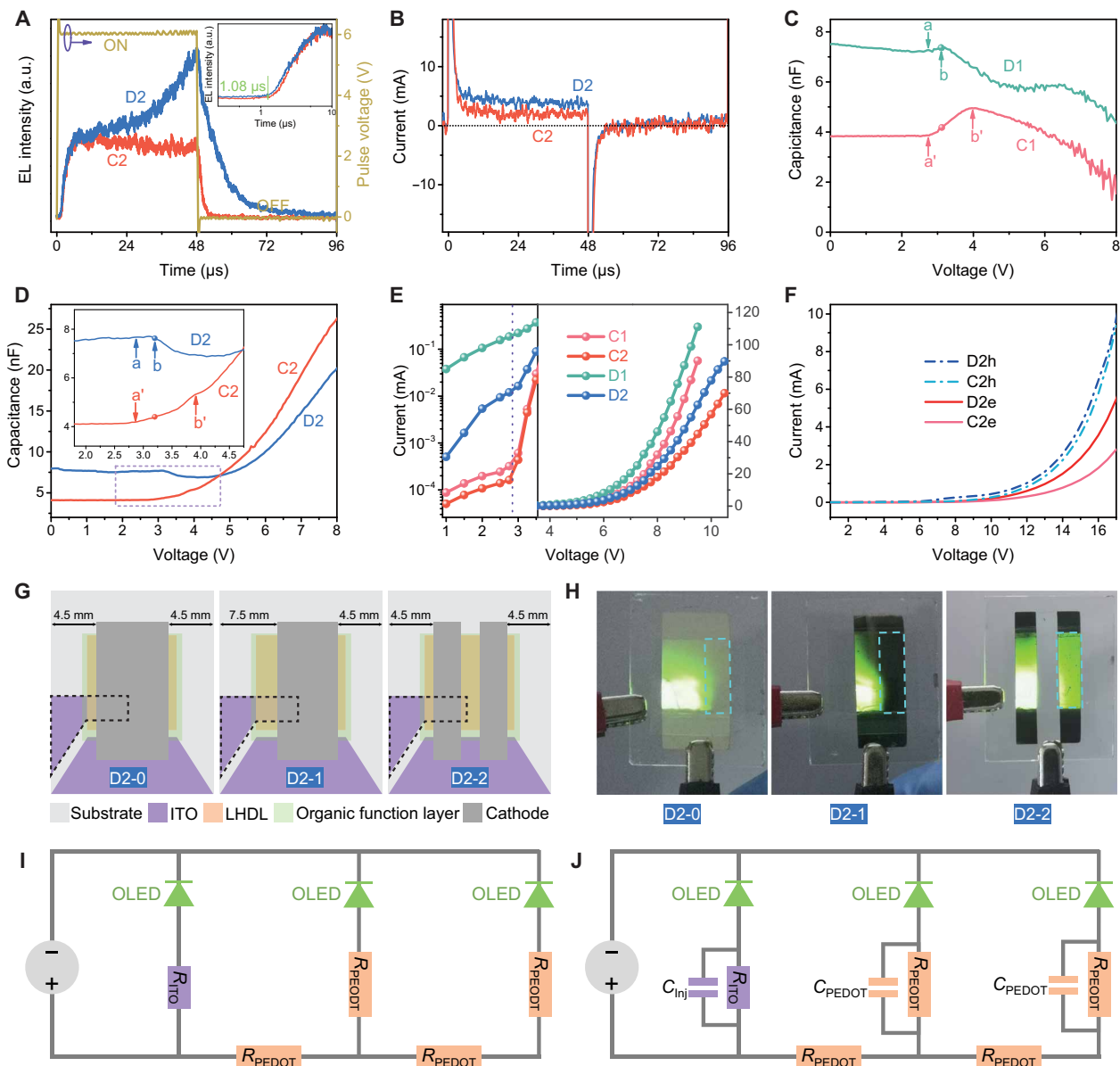
Fig. 3. Lateral hole diffusion behaviors. (**A**) Transient EL responses of devices C2 and D2 and (**B**) their transient current characteristics; the voltage pulse width and heights were, respectively, 48 μs and 6 V. Capacitance-voltage characteristics of (**C**) devices C1 and D1 and (**D**) devices C2 and D2, and the different colors of spheres show their EL onset, respectively. (**E**) Current-voltage characteristics of devices C1, C2, D1, and D2. (**F**) Current-voltage characteristics of single-carrier devices for device C2 and D2 (-e and -h represent electron-only device and hole-only device, respectively). (**G**) Schematic diagrams and (**H**) images of devices D2-0, D2-1, and D2-2 operating at 4 V (the substrate size is 2 cm by 2.5 cm). (**I**) Resistance-dominant and (**J**) capacitance-dominant equivalent circuit models for device D2. a.u., arbitrary units.

$$I_h = I_e + I_L = I_e - qDA\frac{d\rho_{LHDL}}{dx} \qquad (3)$$

The term $-qDA\frac{d\rho_{LHDL}}{dx}$ refers to lateral hole diffusion, and A is the longitudinal cross-section area of the LHDL at the border (dashed line in Fig. 1D) of the ITO-cathode overlapping region.

To further confirm this, capacitance-voltage characteristics of the devices and current-voltage characteristics of their single-carrier devices (fig. S14) were measured. As shown in Fig. 3 (C and D), devices D1 and D2 show much higher geometric capacitance than devices C1 and C2. This is due to highly improved carrier storage ability of the PEDOT:PSS layers upon MeOH treatment (fig. S15 and note S5).

After carrier injection (point a/a' in Fig. 3, C and D and dotted line in Fig. 3E), devices C1 and C2 show capacitance increases from point a' to point b', corresponding to carrier accumulation in the emitting layer (*41*). The capacitance changes in devices D1 (Fig. 3C) and D2 (Fig. 3D) differ considerably from those of devices C1 and C2. It can be seen that upon turning on (at 3.1 V, blue sphere/point b), capacitances of devices D1 and D2 show initial decreases as voltage increases. This gives evidence that current balance in these devices is not solely achieved via carrier accumulation ($I_R = I_h - I_{h'} - \frac{dQ_h}{dt} = I_e$), and the lateral current I_L should work for achieving current balance

$(I_h = I_e + I_L)$. We can observe a brightness enhancement within the ITO-cathode overlapping region of devices D2 and D1 at the same bias voltage (fig. S16). Because of the same working function (fig. S17) of PEDOT:PSS films, the injection currents at the ITO-cathode overlapping regions of devices D2 and D2 is considered to be similar to those of devices C1 and C2. These results thus support the reduction of TPA within and outside the ITO-cathode overlapping region of devices D2 and D1. Furthermore, the lateral diffusion of hole makes it possible for achieving current balance without suppressing hole current. As shown in Fig. 3E, the current of device D2 (D1) is much higher than that of device C2 (C1) under high-bias voltages. According to the voltage-current characteristics (Fig. 3F and fig. S18) of single-carrier devices, the current improvement of devices D2 and D1 is mainly attributed to the improvement in electron current (see I_{eL} in fig. S6C). Besides, Mott-Schottky analyses (fig. S19) also clearly show that devices D2h and C2h show the same built-in potential, while device D2e shows a lower one than device C2e. The results agree well with their current-voltage characteristics.

Working mechanism of an OLED with a LHDL

We further prepare three devices (see the Fig. 3G) for better understanding of the lateral current I_L and its origin. The three devices are prepared by modifying the cathode pattern of device D2 and respectively marked as devices D2-0, D2-1, and D2-2. We can note from Fig. 3H that with the same bias voltage of 4 V, device D2-2 shows emission spreading in the cyan dashed area, while the other devices do not. The emission spreading is proportional to the I_L. The

phenomenon cannot be a resistance-dominant behavior (Fig. 3I), otherwise the I_L should be the same for the cyan dashed areas of the three devices due to parallel circuit characteristics. On the other hand, the phenomenon can be explained by the capacitance-dominant diffusion behavior (Fig. 3J) as proposed in the last section. The I_L will be first injected at the ITO-cathode overlapping area (see the I_{ext} in Fig. 3B) and then diffuse outside (see the delayed rise of Fig. 3A). The diffusion behavior would lead to a constant I_L flowing out of the ITO-cathode area. In devices D2-0 and D2-1, the overall I_L is consumed around the ITO-cathode overlapping area before arriving at the cyan dashed area. When parts of cathode are removed in device D2-2, the I_L can then flow into the cyan dashed area.

As noted above, a working mechanism of the OLEDs with LHDL is proposed and shown in Fig. 4. Compared to electrons, holes are usually more easily injected into the organic layer from anode upon biasing. Because of the highly conductive and capacitive LHDL, excess holes can laterally diffuse outside of the ITO-cathode overlapping region. These diffused holes would then generate an electric field to redistribute electron distribution and assist electron injection from the top cathode. This can explain the observation that device D2 has a much enhanced electron current compared to device C2 (Fig. 3F). Last, the diffused holes and induced electrons form excitons, and photons can be produced from regions both inside and outside of the ITO-cathode overlapping regions. Because of the additional emission from the diffusion area, the total luminescence of device D2 is much higher than that of device C2 (fig. S1b). Because of the reduced hole accumulation in the emitting layer, TPA inside
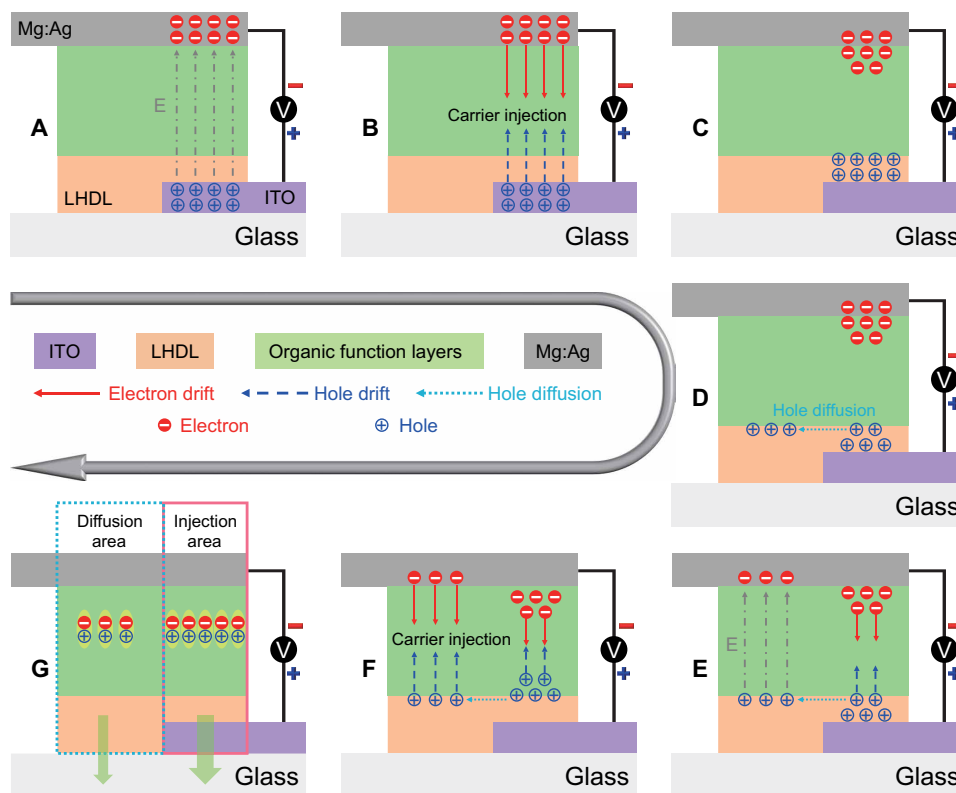

Fig. 4. A working mechanism of an OLED with lateral hole diffusion. (**A**) Applying bias voltage across the anode and cathode. (**B**) Carrier injection in injection area. (**C**) Asymmetric hole and electron transport abilities. (**D**) Hole lateral diffusion. (**E**) Electrical field formation in diffusion area (i.e., area outside ITO-cathode overlapping region). (**F**) Carrier redistribution and injection in diffusion area. (**G**) Exciton recombination radiation.

the ITO-cathode overlapping region is also reduced, thus resulting in a brightness enhancement inside the nominal device region (fig. S16).

OLEDs with LHDL and ITO array anodes

As shown in fig. S20, the emission intensity shows an exponential decay with the distance outside the ITO-cathode overlapping region. This agrees well with the assumption that the lateral current I_L is due to diffusion from the PEDOT:PSS layer (fig. S21 and note S6). To achieve quasi-uniform emission, application of the lateral hole diffusion for OLEDs is then developed by using an array of ITO grid anode (Fig. 5, A to D). Width of and spacing between the ITO fingers

are shown in fig. S22. Device with the structure of device D2 was then fabricated on substrates with the ITO arrays and labeled device D2AA′. For comparison, devices with the structure of device C2 or D2 were respectively fabricated on large-area ITO substrates (Fig. 5E) and marked as device C2LA or D2LA. Devices C2LA and D2LA have the same lighting-emitting area (10 mm by 12 mm; see Fig. 5F) as device D2AA′. Figure 5B shows image (top) of operating device D2AA′. Region marked with green circle is shown as magnified image (bottom). It can be seen that overlapping of spread-out emissions from neighboring ITO finger eventually smooth out the intensity modulation, and the fringe pattern is no longer observable in device D2AA′.
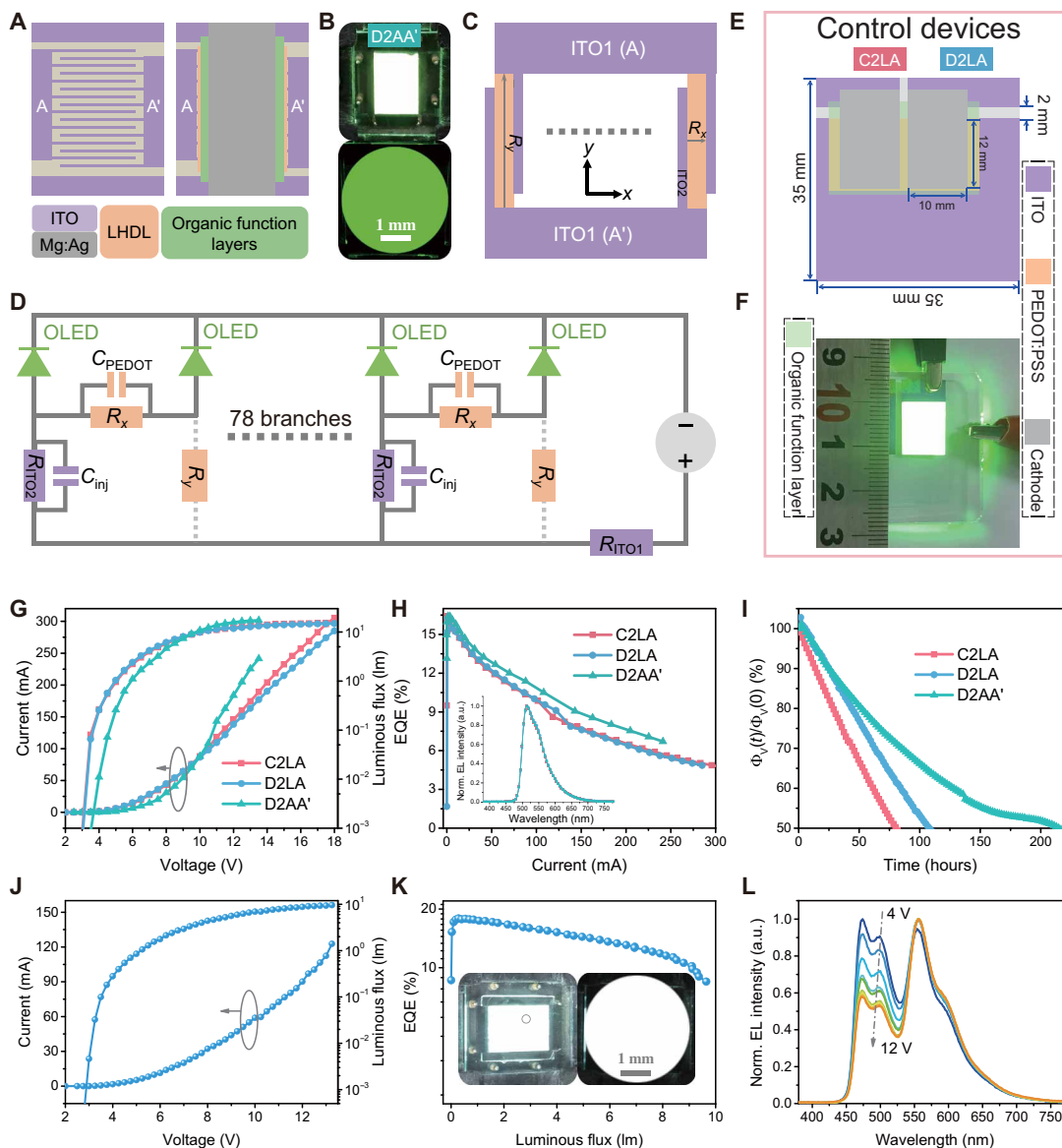

Fig. 5. OLEDs with LHDL and ITO array anodes. (**A**) Schematic diagram of the ITO grid array anode and the corresponding OLED. (**B**) Photographs (top) of operating device D2AA′ with the ITO grid array anodes. Bottom shows magnified images from the green circles marked in the top picture. (**C**) Schematic diagram of anisotropic PEDOT:PSS film. (**D**) Equivalent circuit model of device D2AA′. (**E**) Schematic diagram of the control devices C2LA and D2LA and (**F**) image of the operating device D2LA. (**G**) Current-voltage-luminous flux characteristics, (**H**) EQE-current characteristics and normalized EL spectra, and (**I**) normalized luminous flux degradation $\Phi_v(t)/\Phi_v(0)$ [$\Phi_v(0) = 0.38$ lm] of devices C2LA, D2LA, and D2AA′ with an emitting area of 1.2 cm². (**J**) Current-voltage-luminous flux characteristics, (**K**) EQE-luminous flux characteristics, and (**L**) EL spectra of white device WDAA′ with an emitting area of 1.2 cm²; inset shows its photographs.

Moreover, the impedance spectra (fig. S23) and infrared images (fig. S24) show that the use of long and thin ITO array will not result in increased ITO resistance nor serious thermal effect. This is due to parallel circuit characteristics of this type of ITO electrode and anisotropic transport property of the PEDOT:PSS film (Fig. 5C and fig. S25). The resistance is not a reason for EQE losses but a reason for current limitation (fig. S26). To clarify the issue, the equivalent circuit model of device D2AA′ is presented in Fig. 5D. R_x and R_y, respectively, represent the resistance of the PEDOT:PSS film between two ITO fingers in x and y directions (Fig. 5C). Because of the finger shape, R_y (~8.6 megohm) is four orders of magnitude higher than R_x (~438 ohm). Thus, most current would flow from ITO2 in the x direction to the PEDOT:PSS rather than from ITO1 in the y direction. Besides, the ITO2 has a resistance in kiloohms, but its resistance is still two orders of magnitude lower than those of the small molecular semiconductors on the ITO2 (with an area of 10 mm by 50 μm; see partial area of fig. S25). Considering 80 branches are in parallel with each other (Fig. 5D), the total electrode resistance is dozens of ohms (see the fig. S23).

Figure 5 (G to I) shows EL performances of devices D2AA′, D2LA, and C2LA. Devices D2LA and C2LA show similar luminous flux-voltage-current and EQE-current characteristics. Meanwhile, with the same lighting-emitting area (10 mm by 12 mm), device D2AA′ has much higher EQE than the two devices under high luminous flux (fig. S27) and current (Fig. 5H). The performance improvements of device D2AA′ are not caused by spectra variations (see the inset of Fig. 5H and fig. S28), variations of outcoupling efficiencies (fig. S29), and microcavity effect (fig. S30). Because of the use of large area ITO, lateral hole diffusion behavior is not anticipated in device D2LA. Thus, it should be the lateral hole diffusion that leads to effective reduction of hole accumulation inside the device D2AA′ and thus reduces its efficiency roll-off. Note that this strategy is not specific to the devices above but represents a universal strategy that can be applied in different types of OLEDs (i.e., including blue and red phosphorescent devices and TADF devices) for improving performances (fig. S31).

The hole diffusion layer is also beneficial for improving operational lifetime of phosphorescent OLEDs. The L_{50} lifetime of an OLED is defined as the time it takes until its brightness reaches 50% of the initial value. As shown in Fig. 5I, the LT_{50} lifetime of device D2AA′ can attain 215 hours, which is nearly two times of those devices C2LA and D2LA. Lifetime improvements of the OLEDs with lateral hole diffusion should be attributed to the reduction of exciton-polaron annihilations in these devices, which are well known as the main reason for the short operational lifetime of phosphorescent OLEDs (24). Last, the diffusion layer and the ITO array electrode are applied in a white OLED (called device WDAA′) using bis(3,5-difluoro-2-(2-pyridyl)phenyl-(2-carboxypyridyl) (Firpic) as a blue emitter and bis (4-phenylthieno[3,2-c]pyridinato-$N,C^{2'}$)(acetylacetonate)iridium(III) (PO-01) as a yellow emitter. Figure 5 (J to L) shows EL performances of device WDAA′. Device WDAA′ shows a low efficiency roll-off with the increase of its luminous flux. Considering the above devices, it is reasonably concluded that the lateral hole diffusion plays a role in the efficiency enhancement of WDAA′.

DISCUSSION
Centimeter-scale lateral hole diffusion behavior is observed in a PEDOT:PSS bilayer film that consists of a methanol-treated

PEDOT:PSS layer with high conductivity, which forms a highly capacitive interface with another untreated PEDOT:PSS layer. With this hole diffusion layer, hole injected from the anode can diffuse laterally in centimeter scale away from the anode. This process (i) generates spatial variation of carrier density for balancing carrier injection/transport in the normal emission region defined by the ITO-cathode overlapping area and (ii) induces additional electron injection outside the ITO-cathode overlapping area. These not only lead to a higher luminescence resulting from the spread-out emission but also substantially reduce exciton loss due to polaron-exciton quenching due to the reduced excess hole density at the normal emission region. By combining this hole diffusion layer with an ITO grid array anode, we demonstrate high-performance phosphorescent OLEDs with record-low EQE roll-off at high current and much improved device lifetime.

MATERIALS AND METHODS
Materials
PEDOT:PSS (Clevios P VP AI 4083, Clevios P VP CH 8000) and Ir(ppy)₃ were purchased from Xi'an Polymer Light Technology Corp. PEDOT:PSS (Clevios P VP AI 4083), TAPC, TCTA, CBP, Firpic, PO-01, 5,10-bis(4-(9H-carbazol-9-yl)-2,6-dimethylphenyl)-5,10-dihydroboranthrene (CzDBA), bis(2-methyldibenzo[f,h]quinoxaline)(acetylacetonate)iridium(III) [Ir(MDQ)₂(acac)], TmPyPB, and LiF of OLED grade were purchased from Lumtech Corp. All materials were directly used without further purification.

OLED fabrication
Before using, the PEDOT:PSS aqueous solutions were filtered with 0.45-μm polyamide filters. ITO substrates (25 ohm sq^{-1}) were cleaned by ultrasonic cleaning, dried at 120°C, and then treated with air plasma for 5 min. Using the PEDOT:PSS (Clevios P VP AI 4083) solution, PE4083 films were then spin-coated on the substrate at 5000 rpm for 30 s, followed by annealing at 120°C for 10 min. After that, some PE4083 films were soaked in methanol at 60°C for 10 min and referred to as PE4083-MeOH films. To obtain PE4083/PE8000 and PE4083-MeOH/PE8000 films, PE8000 films were then spin-coated on the PE4083 and PE4083-MeOH films at 5000 rpm for 30 s using PEDOT:PSS (Clevios P VP CH 8000) solution, followed by annealing at 120°C for 10 min. All the small molecular function layers and cathode were then deposited in turn on the PEDOT:PSS–coated substrates via thermal evaporation. Evaporating rates of the organic materials, LiF, and Mg:Ag are 1 to 2, 0.05 to 0.1, and 2 to 3 Å/s, respectively.

Device measurements and film characterizations
EL performances of all OLEDs were measured in atmosphere at room temperature. Spectral flux $\Phi_{e\lambda}$ (W/nm) emitted from the OLEDs in the forward direction was measured using a commercial goniophotometric measurement system (Otsuka Electronics, Japan) consisting of a Keithley 2400 source, a MCPD 9800 spectrometer, an integrated sphere, and a light-receiving fiber. Performance parameters not related to light-emitting area are obtained as

$$\Phi_v = K_m \int_{380}^{780} V(\lambda)\,\Phi_{e\lambda}\,d\lambda,$$

$$I_v = \frac{\partial \Phi_v}{\partial \Omega},$$

$$\mathrm{CE} \ = \ \frac{I_{\mathrm{v}}}{I},$$

$$\mathrm{PE} \ = \ \frac{\Phi_{\mathrm{v}}}{I \cdot V},$$

$$\mathrm{EQE} \ = \ \frac{\pi q}{\mathrm{h} c \cdot I} \int_{380}^{780} \lambda\, \Phi_{e\lambda}\, d\lambda$$

where Φ_{v} (lm) is the luminous flux, I_{v} (cd) is the luminous intensity, CE (cd/A) is the current efficiency, PE (lm/W) is the power efficiency, K_{m} is the maximum spectral luminous efficiency, $V(\lambda)$ is the luminosity function, λ is the wavelength, Ω is the solid angle, I is the current, V is the bias voltage, q is the elementary charge, h is the Planck's constant, and c is the speed of light. Devices in this work are Lambertian sources. For Lambertian surfaces with spatially homogeneous emission, a factor of π sr is used to relate luminance to illuminance, radiant intensity to radiant flux, and radiance to radiant emittance.

These parameters were synchronously determined with a measurement software from Otsuka Electronics, Japan. The brightness L_{v} (cd/m^2) is related to light-emitting area

$$L_{\mathrm{v}} = \frac{d\Phi_{\mathrm{v}}}{d\Omega \mathrm{dS} \cos\theta}$$

where dS is an infinitesimal area of the light source containing the specified point, and θ is the angle between the normal $n_{\mathbf{S}}$ to the surface dS and the specified direction. The brightness of the ITO-cathode overlapping area of devices D1 and D2 is measured with a brightness meter LS-110 Brightness Meter (Konica Minolta, Japan) targeted to a ~0.4-mm-diameter spot at an ITO-cathode overlapping area. The nominal brightness of white devices is measured by the goniophotometric measurement system using the sum of injection area and diffusion area as the light-emitting area of devices with LHDL and using the ITO-cathode overlapping area as the light-emitting area of devices without LHDL. Transient EL response was collected with a SPCS-T01 Fluorescence Spectrum Analyzer System (Beijing HOLITA, China). Impedance spectra and capacitance-voltage characteristics were measured with a ZAHNER IM6 and a HP44284A semiconductor analyzer.

SUPPLEMENTARY MATERIALS

Supplementary material for this article is available at https://science.org/doi/10.1126/sciadv.abm1999

View/request a protocol for this paper from *Bio-protocol*.

REFERENCES AND NOTES

1. M. A. Fusella, R. Saramak, R. Bushati, V. M. Menon, M. S. Weaver, N. J. Thompson, J. J. Brown, Plasmonic enhancement of stability and brightness in organic light-emitting devices. *Nature* **585**, 379–382 (2020).
2. J. Song, H. Lee, E. G. Jeong, K. C. Choi, S. Yoo, Organic light-emitting diodes: Pushing toward the limits and beyond. *Adv. Mater.* **32**, 1907539 (2020).
3. Y. Xu, P. Xu, D. Hu, Y. Ma, Recent progress in hot exciton materials for organic light-emitting diodes. *Chem. Soc. Rev.* **50**, 1030–1069 (2021).
4. C.-Y. Chan, M. Tanaka, Y.-T. Lee, Y.-W. Wong, H. Nakanotani, T. Hatakeyama, C. Adachi, Stable pure-blue hyperfluorescence organic light-emitting diodes with high-efficiency and narrow emission. *Nat. Photonics* **15**, 203–207 (2021).
5. S. O. Jeon, K. H. Lee, J. S. Kim, S.-G. Ihn, Y. S. Chung, J. W. Kim, H. Lee, S. Kim, H. Choi, J. Y. Lee, High-efficiency, long-lifetime deep-blue organic light-emitting diodes. *Nat. Photonics* **15**, 208–215 (2021).
6. M. Choi, S.-R. Bae, L. Hu, A. T. Hoang, S. Y. Kim, J.-H. Ahn, Full-color active-matrix organic light-emitting diode display on human skin based on a large-area MoS$_2$ backplane. *Sci. Adv.* **6**, eabb5898 (2020).
7. B. S. Karunathilaka, U. Balijapalli, C. A. Senevirathne, S. Yoshida, Y. Esaki, K. Goushi, T. Matsushima, A. S. Sandanayaka, C. Adachi, Suppression of external quantum efficiency rolloff in organic light emitting diodes by scavenging triplet excitons. *Nat. Commun.* **11**, 4926 (2020).
8. L. Cao, K. Klimes, Y. Ji, T. Fleetham, J. Li, Efficient and stable organic light-emitting devices employing phosphorescent molecular aggregates. *Nat. Photonics* **15**, 230–237 (2021).
9. C. Murawski, K. Leo, M. C. Gather, Efficiency roll-off in organic light-emitting diodes. *Adv. Mater.* **25**, 6801–6827 (2013).
10. N. C. Giebink, S. Forrest, Quantum efficiency roll-off at high brightness in fluorescent and phosphorescent organic light emitting diodes. *Phys. Rev. B* **77**, 235215 (2008).
11. J.-L. Brédas, J. P. Calbert, D. da Silva Filho, J. Cornil, Organic semiconductors: A theoretical characterization of the basic parameters governing charge transport. *Proc. Natl. Acad. Sci. U.S.A.* **99**, 5804–5809 (2002).
12. L.-S. Cui, S.-B. Ruan, F. Bencheikh, R. Nagata, L. Zhang, K. Inada, H. Nakanotani, L.-S. Liao, C. Adachi, Long-lived efficient delayed fluorescence organic light-emitting diodes using n-type hosts. *Nat. Commun.* **8**, 2250 (2017).
13. L. Hassine, H. Bouchriha, J. Roussel, J.-L. Fave, Transient response of a bilayer organic light emitting diode: Building-up of external and recombination currents. *J. Appl. Phys.* **91**, 5170–5175 (2002).
14. H. Aziz, Z. D. Popovic, N.-X. Hu, A.-M. Hor, G. Xu, Degradation mechanism of small molecule-based organic light-emitting devices. *Science* **283**, 1900–1902 (1999).
15. A. Obolda, Q. Peng, C. He, T. Zhang, J. Ren, H. Ma, Z. Shuai, F. Li, Triplet-polaron-interaction-induced upconversion from triplet to singlet: A possible way to obtain highly efficient OLEDs. *Adv. Mater.* **28**, 4740–4746 (2016).
16. Y. Zhang, D. Zhang, T. Tsuboi, Y. Qiu, L. Duan, Simultaneous enhancement of efficiency and stability of OLEDs with thermally activated delayed fluorescence materials by modifying carbazoles with peripheral groups. *Sci. China Chem.* **62**, 393–402 (2019).
17. J. S. Bangsund, J. R. Van Sambeek, N. M. Concannon, R. J. Holmes, Sub–turn-on exciton quenching due to molecular orientation and polarization in organic light-emitting devices. *Sci. Adv.* **6**, eabb2659 (2020).
18. M. Du, Y. Feng, D. Zhu, T. Peng, Y. Liu, Y. Wang, M. R. Bryce, Novel emitting system based on a multifunctional bipolar phosphor: An effective approach for highly efficient warm-white light-emitting devices with high color-rendering index at high luminance. *Adv. Mater.* **28**, 5963–5968 (2016).
19. Y. Miao, K. Wang, L. Gao, B. Zhao, H. Wang, F. Zhu, B. Xu, D. Ma, Precise manipulation of the carrier recombination zone: A universal novel device structure for highly efficient monochrome and white phosphorescent organic light-emitting diodes with extremely small efficiency roll-off. *J. Mater. Chem. C* **8**, 8122–8134 (2018).
20. M. Einzinger, T. Zhu, P. de Silva, C. Belger, T. M. Swager, T. Van Voorhis, M. A. Baldo, Shorter exciton lifetimes via an external heavy-atom effect: Alleviating the effects of bimolecular processes in organic light-emitting diodes. *Adv. Mater.* **29**, 1701987 (2017).
21. F. Zhao, Y. Wei, H. Xu, D. Chen, T. Ahamad, S. Alshehri, Q. Pei, D. Ma, Spatial exciton allocation strategy with reduced energy loss for high-efficiency fluorescent/phosphorescent hybrid white organic light-emitting diodes. *Mater. Horiz.* **4**, 641–648 (2017).
22. C. Zang, S. Liu, M. Xu, R. Wang, C. Cao, Z. Zhu, J. Zhang, H. Wang, L. Zhang, W. Xie, C. Lee, Top-emitting thermally activated delayed fluorescence organic light-emitting devices with weak light-matter coupling. *Light Sci. Appl.* **10**, 116 (2021).
23. X. Li, J. Cui, Q. Ba, Z. Zhang, S. Chen, G. Yin, Y. Wang, B. Li, G. Xiang, K. S. Kim, H. Xu, Z. Zhang, H.-L. Wang, Multiphotoluminescence from a triphenylamine derivative and its application in white organic light-emitting diodes based on a single emissive layer. *Adv. Mater.* **31**, e1900613 (2019).
24. J. Lee, C. Jeong, T. Batagoda, C. Coburn, M. E. Thompson, S. R. Forrest, Hot excited state management for long-lived blue phosphorescent organic light-emitting diodes. *Nat. Commun.* **8**, 15566 (2017).
25. Q. Burlingame, C. Coburn, X. Che, A. Panda, Y. Qu, S. R. Forrest, Centimetre-scale electron diffusion in photoactive organic heterostructures. *Nature* **554**, 77–80 (2018).
26. S. R. Forrest, *Organic Electronics: Foundations to Applications* (Oxford Univ. Press, 2020), pp. 234–236.
27. N. B. Kotadiya, H. Lu, A. Mondal, Y. Ie, D. Andrienko, P. W. M. Blom, G.-J. A. Wetzelaer, Universal strategy for Ohmic hole injection into organic semiconductors with high ionization energies. *Nat. Mater.* **17**, 329–334 (2018).
28. B.-Q. Liu, L. Wang, D.-Y. Gao, J.-H. Zou, H.-L. Ning, J.-B. Peng, Y. Cao, Extremely high-efficiency and ultra-simplified hybrid white organic light-emitting diodes exploiting double multifunctional blue emitting layers. *Light Sci. Appl.* **5**, e16137 (2016).

29. Y. Li, M. Kovačič, J. Westphalen, S. Oswald, Z. Ma, C. Hänisch, P.-A. Will, L. Jiang, M. Junghaehnel, R. Scholz, Tailor-made nanostructures bridging chaos and order for highly efficient white organic light-emitting diodes. *Nat. Commun.* **10**, 2972 (2019).

30. L. Berger, Exchange interaction between ferromagnetic domain wall and electric current in very thin metallic films. *J. Appl. Phys.* **55**, 1954–1956 (1984).

31. C. Coburn, D. Fan, S. R. Forrest, Organic charge-coupled device. *ACS Photonics* **6**, 2090–2095 (2019).

32. I. Slowik, A. Fischer, S. Gutsche, R. Brückner, H. Fröb, S. Lenk, S. Reineke, K. Leo, New concept for organic light-emitting devices under high excitations using emission from a metal-free area (SPIE Photonics Europe, SPIE, 2016), vol. 9895.

33. I. Slowik, A. Fischer, H. Fröb, S. Lenk, S. Reineke, K. Leo, Novel organic light-emitting diode design for future lasing applications. *Org. Electron.* **48**, 132–137 (2017).

34. Z. Wu, Y. Liu, L. Yu, C. Zhao, D. Yang, X. Qiao, J. Chen, C. Yang, H. Kleemann, K. Leo, D. Ma, Strategic-tuning of radiative excitons for efficient and stable fluorescent white organic light-emitting diodes. *Nat. Commun.* **10**, 2380 (2019).

35. X. Tang, X. Y. Liu, Z. Q. Jiang, L. S. Liao, High-quality white organic light-emitting diodes composed of binary emitters with color rendering index exceeding 80 by utilizing color remedy strategy. *Adv. Funct. Mater.* **29**, 1807541 (2019).

36. S. F. Wu, S. H. Li, Y. K. Wang, C. C. Huang, Q. Sun, J. J. Liang, L. S. Liao, M. K. Fung, White organic LED with a luminous efficacy exceeding 100 lm W^{-1} without light out-coupling enhancement techniques. *Adv. Funct. Mater.* **27**, 1701314 (2017).

37. L. Hassine, H. Bouchriha, J. Roussel, J.-L. Fave, Transient response of a bilayer organic electroluminescent diode: Experimental and theoretical study of electroluminescence onset. *Appl. Phys. Lett.* **78**, 1053–1055 (2001).

38. A. V. Volkov, K. Wijeratne, E. Mitraka, U. Ail, D. Zhao, K. Tybrandt, J. W. Andreasen, M. Berggren, X. Crispin, I. V. Zozoulenko, Understanding the capacitance of PEDOT: PSS. *Adv. Funct. Mater.* **27**, 1700329 (2017).

39. D. Alemu, H.-Y. Wei, K.-C. Ho, C.-W. Chu, Highly conductive PEDOT: PSS electrode by simple film treatment with methanol for ITO-free polymer solar cells. *Energ. Environ. Sci.* **5**, 9662–9671 (2012).

40. A. Lasia, Electrochemical impedance spectroscopy and its applications, in *Modern Aspects of Electrochemistry* (Springer, 2002), pp. 143–248.

41. J. H. Lee, S. Lee, S. J. Yoo, K. H. Kim, J. J. Kim, Langevin and trap-assisted recombination in phosphorescent organic light emitting diodes. *Adv. Funct. Mater.* **24**, 4681–4688 (2014).

42. S. Wang, X. Wang, B. Yao, B. Zhang, J. Ding, Z. Xie, L. Wang, Solution-processed phosphorescent organic light-emitting diodes with ultralow driving voltage and very high-power efficiency. *Sci. Rep.* **5**, 12487 (2015).

43. T.-H. Han, M.-R. Choi, C.-W. Jeon, Y.-H. Kim, S.-K. Kwon, T.-W. Lee, Ultrahigh-efficiency solution-processed simplified small-molecule organic light-emitting diodes using universal host materials. *Sci. Adv.* **2**, e1601428 (2016).

44. M. Ramar, P. Tyagi, C. K. Suman, R. Srivastava, Enhanced carrier transport in tris (8-hydroxyquinolinate) aluminum by titanyl phthalocyanine doping. *RSC Adv.* **4**, 51256–51261 (2014).

45. J. Li, B. Qiao, S. Zhao, D. Song, C. Zhang, Z. Xu, Investigation on OLEDs efficiency roll-off with interfacial charge storage and their time-resolved emission spectra. *Org. Electron.* **83**, 105756 (2020).

46. D. Khramtchenkov, H. Bässler, V. Arkhipov, A model of electroluminescence in organic double-layer light-emitting diodes. *J. Appl. Phys.* **79**, 9283–9290 (1996).

47. V. Nikitenko, V. Arkhipov, Y.-H. Tak, J. Pommerehne, H. Bässler, H.-H. Hörhold, The overshoot effect in transient electroluminescence from organic bilayer light-emitting diodes: Experiment and theory. *J. Appl. Phys.* **81**, 7514–7525 (1997).

48. L. Zhang, H. Nakanotani, C. Adachi, Capacitance-voltage characteristics of a 4, 4′-bis [(*N*-carbazole) styryl] biphenyl based organic light-emitting diode: Implications for characteristic times and their distribution. *Appl. Phys. Lett.* **103**, 093301 (2013).

49. J. H. Lee, J. Kim, G. Kim, D. Shin, S. Y. Jeong, J. Lee, S. Hong, J. W. Choi, C. L. Lee, H. Kim, Y. Yi, Introducing paired electric dipole layers for efficient and reproducible perovskite solar cells. *Energ. Environ. Sci.* **11**, 1742–1751 (2018).

50. K. A. Neyts, Simulation of light emission from thin-film microcavities. *J. Opt. Soc. Am. A* **15**, 962–971 (1998).

51. M. Furno, R. Meerheim, S. Hofmann, B. Lüssem, K. Leo, Efficiency and rate of spontaneous emission in organic electroluminescent devices. *Phys. Rev. B* **85**, 115205 (2012).